# Validation of NCAR 10.6-$\mu$m $CO_2$ Doppler Lidar Radial Velocity Measurements and Comparison with a 915-MHz Profiler

SHANE D. MAYOR AND DONALD H. LENSCHOW

*National Center for Atmospheric Research, Boulder, Colorado*

RONALD L. SCHWIESOW

*Ball Aerospace and Technology Corporation, Boulder, Colorado*

JAKOB MANN

*Risø National Laboratory, Roskilde, Denmark*

CHARLES L. FRUSH

*National Center for Atmospheric Research, Boulder, Colorado*

MELINDA K. SIMON

*National Oceanic and Atmospheric Administration, Boulder, Colorado*

(Manuscript received 18 January 1996, in final form 11 January 1997)

ABSTRACT

The capability of the NCAR 10.6-$\mu$m-wavelength $CO_2$ Doppler lidar to measure radial air motion is validated by examining hard-target test data, comparing measurements with those from a two-axis propeller anemometer and a 915-MHz profiling radar, and analyzing power spectra and autocovariance functions of the lidar radial velocities in a daytime convective boundary layer. Results demonstrate that the lidar is capable of measuring radial velocity to less than 0.5 m $s^{-1}$ precision from 20 laser pulse averages under high signal-to-noise ratio conditions. Hard-target test data and comparisons with other sensors show that the lidar data can be biased by as much as $\pm 2$ m $s^{-1}$ when operating in the coherent oscillator mode and that correlated errors are negligible. Correlation coefficients are as large as 0.96 for 90-min comparisons of horizontal velocities averaged for 1 min from the lidar and anemometer, and 0.87 for 2.5-h comparisons between vertical velocities averaged for 30 s from the lidar and profiler. Comparisons of the lidar and profiler vertical velocities are particularly encouraging for the profiler since these results show that 915-MHz profilers are capable of making good vertical velocity measurements in strong convective boundary layers. The authors conclude that despite the commonplace systematic bias in lidar radial velocity, ground-based operation of the NCAR $CO_2$ Doppler lidar can provide valuable velocity data for meso- and microscale meteorological studies. The lidar can also provide filtered velocity statistics that may be useful for boundary layer turbulence research.

## 1. Introduction

To date, several Doppler lidars that operate near the 10-$\mu$m wavelength have been shown to measure wind fields in cloud- and precipitation-free conditions over the mesogamma (approximately 20 to 2 km) to microbeta (approximately 200 to 2 m) scales of atmospheric motion (Orlanski 1975). These include the NOAA-ETL ground-based system (Post and Cupp 1990), the NASA Airborne Doppler Lidar System (ADLS) (Bilbro et al. 1986; Bilbro et al. 1984), the NOAA-ETL mini-MOPA (Brewer and Hardesty 1995), and the NCAR $CO_2$ Doppler lidar (Schwiesow and Spowart 1996).

Mesoscale applications of the NOAA-ETL ground-based Doppler lidar (Banta et al. 1993a) include observing frontal structure (Neiman et al. 1988a) and studying the airflow in the vicinity of a forest fire (Banta et al. 1992), sea-breeze circulations (Banta et al. 1993b), downslope windstorms (Neiman et al. 1988b; Banta et al. 1990), airflow in the Grand Canyon (Banta et al. 1991), mountain valley flow (Post and Neff 1986), and thunderstorm outflows (Intrieri et al. 1990). Rothermel et al. (1985) report on dual-Doppler lidar measurements

*Corresponding author address:* Shane D. Mayor, Dept. of Atmospheric and Oceanic Sciences, University of Wisconsin—Madison, 1225 W. Dayton St., Madison, WI 53706-1695.
E-mail: shane@lidar.ssec.wisc.edu

of mesoscale wind fields during the Joint Airport Weather Studies (JAWS) Project. The NASA ADLS was used by Blumen and Hart (1988) to measure the wind field in the lee waves of Mount Shasta and by McCaul et al. (1986) to measure the wind field in the vicinity of severe thunderstorms. In 1995, the NOAA ground-based system was installed in a NASA DC-8 aircraft for airborne application (Rothermel et al. 1995).

Microscale applications of the NOAA-ETL ground-based Doppler lidar include Eberhard et al. (1989) and Gal-Chen et al. (1992), who studied convective boundary layer turbulence structure. Lee (1983) used data from the NASA ADLS for a qualitative comparison of the horizontal flow patterns in and just above the boundary layer. Cliff and Skarda (1987) computed lateral and longitudinal turbulence length scales from NASA ADLS-measured horizontal wind fields at 600 and 800 m above ground level (AGL) near Palm Springs, California.

Because of this demonstrated utility of both ground-based and airborne Doppler lidars that operate near the 10-$\mu$m wavelength, NCAR undertook the development of a heterodyne pulsed $CO_2$ lidar system, compactly designed for airborne deployment, which underwent extensive ground-based testing in 1994 and 1995. This lidar has been known as the NCAR Airborne Infrared Lidar System (NAILS). However, we do not refer to it as NAILS here since it has not been used on an aircraft for velocity measurements. Here, we validate its capability to measure radial air velocity from the ground with good signal-to-noise ratio (SNR) (i.e., adequate backscattered power). We begin by presenting radial velocity estimates of a stationary target and show how the random error in the estimates is a function of SNR and that correlated errors in the velocity estimates are negligible. We then compare near-horizontal lidar radial velocities at the 1.5-km range with the horizontal wind speed component parallel to the lidar line of sight from a tower-mounted Portable Automated Mesonet II (PAM II) (Militzer 1987) two-axis propeller anemometer. Next, we compare lidar-derived vertical velocities at multiple altitudes with those from a nearby 915-MHz radar (Ecklund et al. 1988). Last, we compare spatial and temporal radial velocity statistics using power spectra and autocovariance functions of 2D (time versus range) radial velocity fields. All the data analyzed were collected with the lidar beam fixed in either an almost-horizontal or a vertical direction (Mayor 1995 and Mayor et al. 1995).

Previous work validating Doppler lidar measurements using fixed beams includes Benedetti-Michelangeli et al. (1972) and Congeduti et al. (1981), who used an $Ar^+$ laser (0.4880-$\mu$m wavelength) transmitter and a Fabry–Perot interferometer for signal processing. The first paper compared the lidar radial velocity in the west-to-east direction with wind speeds from a nearby rawinsonde. The second compared lidar vertical velocities at multiple altitudes to those from a Doppler sodar. Post et al. (1978) and Hardesty and Weber (1987) also used the fixed-beam technique with continuous-wave $CO_2$ Doppler lidars that measure radial velocity at only one range, in contrast to pulsed lidars, which provide range-resolved measurements.

Hall et al. (1984) report on the wind measurement accuracy of the NOAA pulsed $CO_2$ heterodyne Doppler lidar; however, they employ velocity–azimuth display (VAD) scanning (Kropfli 1986; Eberhard et al. 1989) to measure horizontal wind profiles from the lidar for comparisons with anemometers, rawinsondes, Jimspheres, and a 50-MHz radar profiler. Lawrence et al. (1986) also compare ground-based Doppler lidar measurements of horizontal winds derived from VAD scanning with those from a 915-MHz profiler and rawinsondes. The VAD method of azimuthal scanning at a constant elevation angle is good for estimating mean profiles of horizontal wind speed and direction but does not provide continuous time series of a single component for comparison with other sensors.

Eilts et al. (1984) compare NASA ALDS measurements of horizontal wind with those from dual-Doppler radars and tower anemometers. The lidar winds were computed by alternating the beam angle from 20° forward to 20° aft of a line normal to the aircraft centerline. This technique requires substantial spatial averaging of the data and its accuracy is affected by errors in the aircraft's inertial navigation system and by a varying wind field between the two intersecting measurements of the same volume (Carroll 1986).

Kavaya et al. (1989) and Hawley et al. (1993) report on the development and application of Nd:YAG-based solid-state Doppler lidars at 1-$\mu$m and compare lidar horizontal winds with rawinsonde observations. Henderson et al. (1991), Grund and Post (1992), Henderson et al. (1993), Hannon and Thomson (1994), Frehlich et al. (1994), and Hannon and Henderson (1995) report on solid-state systems that operate near the 2-$\mu$m wavelength, and Hannon and Henderson (1995) compare lidar radial velocities with those from a shuttle landing. Frehlich et al. (1994) also use the fixed-beam approach for performance analysis of a 2-$\mu$m Doppler lidar but do not compare the measurements with those from other sensors.

A disadvantage of 1-$\mu$m lidars is that they are not eye-safe. However, 2-$\mu$m lidars are eye-safe and feature shorter pulses, less chirp, and higher pulse repetition frequencies than 10-$\mu$m $CO_2$ lidars. Shorter-wavelength lidars have the advantages (Kavaya et al. 1989) of better range resolution for an equivalent wind-velocity resolution, compactness, and room-temperature detectors. On the other hand, 10-$\mu$m lidars are able to operate with higher heteordyne efficiency for a given telescope aperture due to less coherency degradation from refractive index inhomogeneities. Furthermore, detector and processor bandwidths are less for longer-wavelength systems. Menzies (1986) and Frehlich et al. (1995) compare the performance of 2- and 10-$\mu$m Doppler lidars.

## 2. Description of the NCAR 10-$\mu$m $CO_2$ Doppler lidar

Schwiesow and Spowart (1996) provide a detailed description of the NCAR $CO_2$ Doppler lidar. In this section we describe the lidar briefly and comment on its uniqueness. Because the NCAR Doppler lidar was intended for airborne use, it is more compact than the NOAA-ETL ground-based Doppler lidar, which also uses an injection-seeded $CO_2$ transverse-excitation atmospheric-pressure (TEA) laser to generate pulses. The NCAR lidar's smaller size and weight is achieved by using a shorter TEA laser cavity (0.63 m instead of 3.1 m) and only a single local oscillator (LO). Longer cavities reduce pulse chirp but require heavier substrates to maintain rigidness. The use of two LOs allows independent TEA seeding and optical heteordyning; however, the NCAR LO serves as both a seed for the TEA and a source of reference frequency by employing a Faraday isolator that prevents the transmit pulses from disturbing the LO.

The TEA laser is constrained to transmit approximately 10 MHz lower than the frequency of the LO that is tuned to the peak of the 10.6-$\mu$m line of the $CO_2$ molecule. Optically heterodyning the transmit pulse with output from the LO produces an intermediate frequency (IF) of approximately 10 MHz that is bandpass filtered from 5 to 15 MHz. The optically heterodyned signal is then mixed with a radio-frequency (RF) oscillator at approximately 10 MHz to produce in-phase ($I$) and quadrature ($Q$) components from 0 to 5 MHz in order to use two digitizers with sample rates of $10^7$ samples per second.

The NCAR Doppler lidar can transmit 100–200-mJ pulses at 10.6-$\mu$m wavelength (28.3 THz) at a pulse repetition frequency (PRF) of 10 or 20 $s^{-1}$. The transmitted pulse length and power depend on the mixing ratio of helium, nitrogen, and carbon dioxide in the TEA laser; here, we used a 3:2:1 mixture by volume. The lidar is most sensitive to particles with diameters of 2 to 6 $\mu$m (Post 1978). Backscatter is Doppler shifted 189 kHz per meter per second of radial air motion with respect to the lidar.

Due to detector saturation, atmospheric data are unavailable for the first few microseconds after the laser pulse is transmitted. Digitization of the Doppler-shifted backscatter begins at 4 $\mu$s (600 m) and extends to 10 km in 15-m increments. The lidar can resolve two distinct scattering features approximately 100 m apart. This axial resolution limit is determined by the laser pulse length.

The velocity measurement range of the lidar is limited by electronic filtering of the IF signal. This filtering is designed to match the analog-to-digital sampling at a 10-MHz rate to provide a passband of 5 to 15 MHz. This results in an unambiguous velocity range of $\pm 26$ m $s^{-1}$ with filtering to remove frequencies outside this range. Radial velocities outside this range would have a negligible influence on the velocity measurements. We note that aliasing in a Doppler lidar is controlled by digitization rate. Higher digitization rates would extend the unambiguous velocity range of the lidar.

A disadvantage of using only one LO appears to be the formation of a parasitic interferometer caused by two parallel optical surfaces in the system of which at least one is in the Faraday isolator. The parasitic interferometer induces variability in the LO signal on the chilled detector, which affects system gain. Obtaining a precise optical alignment to minimize the variability is difficult. We suspect the variations are induced by thermal contractions and expansions of the lidar chassis. However, the effect can be minimized by carefully adjusting several optical components.

The radial velocities analyzed in this paper were estimated using single-lag complex autocovariance processing (Doviak and Zrnić 1993; Zrnić 1979; Keeler and Passarelli 1990). This technique, also known as pulse-pair processing, operates on a complex time series of $I$ and $Q$ signals. Sirmans and Bumgarner (1975) and Frehlich and Yadlowsky (1994) discuss the performance of mean frequency estimators. The atmospheric coherence time (Doviak and Zrnić 1993) for a lidar (approximately 1 $\mu$s for a 10-$\mu$m lidar) is so short that velocity must be estimated from the backscatter from a single laser pulse. For this reason we process the $I$ and $Q$ data from several (usually 7 to 15) adjacent spatial pairs corresponding to the transmitted pulse length to obtain velocity estimates within the coherence time. Although independent radial velocity estimates are separated in range by approximately 200 m, we move the complex autocovariance processing function in range to provide radial velocity estimates every 15 m.

All the lidar data presented in this paper were collected while the lidar was operating at 10-Hz PRF. For example, to provide 1-s temporal resolution data, we accumulate separately the zero and first lag vectors of 10 consecutive complex autocovariance functions. The angle between the accumulated vector and the real axis is proportional to the mean radial velocity over the gates used. For the data presented in this paper no additional filtering or smoothing was applied in time or range.

The lidar beam is 30 cm in diameter and collimated for approximately the first 4 km of range. Beyond 4 km, the beam diverges at approximately 80 $\mu$rad full angle due to diffraction. This amounts to an 8-cm increase in beam diameter for each kilometer of range beyond 4 km. The small beam divergence and absence of sidelobes allow measurements at low elevation angles.

Figure 1 shows the heterodyne beat frequency when the TEA pulse is mixed with output from the LO. Most of the energy is contained in the first microsecond of the pulse with a subsequent, relatively gradual, decay. The beat frequency (approximately 10 MHz) is not constant through the duration of the pulse. This so-called chirp (approximately 10 MHz per microsecond) is due

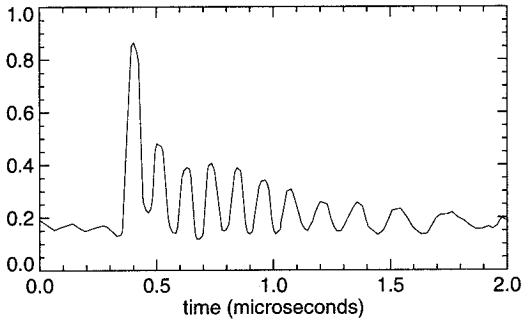


FIG. 1. Transmit pulse optically heteordyned with the LO that provides the reference beat frequency.

to two effects inside the TEA laser (Willets and Harris 1982). The first is the decay of free electrons in the TEA discharge plasma, which produces an increasing frequency at the beginning of the pulse. The second effect, which decreases the frequency throughout the remainder of the pulse, is due to laser-induced refractive index perturbations.

The effect of pulse chirp on the velocity measurement becomes significant when large scattering gradients are present in the atmosphere. Usually, scatterers are well mixed in the turbulent boundary layer. However, when distinct plumes of particulates exist (such as smoke or effluent from an exhaust stack or roadway, or dust from a construction or farm site), the chirp coupled with the sharp gradient in scattering causes a characteristic signature in the radial velocity profile in the vicinity of the scattering gradient. The atmospheric data analyzed in this paper have been selected where this effect is a minimum.

The *I* and *Q* data used in the current study were collected using a so-called coherent oscillator (CohO) mode of operation. This technique employs an analog electronic frequency discriminator to estimate the difference in frequency between a point on the transmit pulse and LO in real time and adjust the frequency of the RF oscillator used to generate *I* and *Q* components for each pulse so that zero frequency of *I* and *Q* corresponds to zero velocity. This unique dynamic approach can be contrasted with the so-called stable local oscillator (StaLO) mode of operation in which the RF oscillator is fixed at 10 MHz. The NOAA $CO_2$ Doppler lidar utilizes the StaLO technique. In the StaLO case, velocity estimates for each pulse need to be corrected for the departures of the IF from 10 MHz on a pulse-by-pulse basis. The advantage of the CohO is that such corrections are automatic and keep the IF signal centered in the bandpass of the processing electronics. The disadvantage is the difficulty in making an accurate estimate of the difference frequency between the TEA and LO when the TEA pulse exhibits variable chirp.

## 3. Hard-target testing

To determine both the random and correlated errors in the radial velocity measurement, the Doppler lidar was pointed at a stationary sandpaper target at the 2.78-km range. By directing the lidar beam slightly above the sandpaper target, we could also gather data returned from the terrain at the 7.75-km range.

To carefully measure characteristics of the lidar pulse (such as spectral width), we digitized the IF signal at 60 MHz and 12-bit resolution with a digitizer card in a PC. Although the lidar was running with a PRF of 10 Hz, the digitizer and PC combination were only able to record one pulse approximately every 2 s. We digitized and saved waveforms from 6.7 $\mu$s before to 34 $\mu$s after the laser fired. This provided us with background information, as well as reference frequency information, atmospheric velocity between the lidar and the target, and a mirror image of the lidar pulse from the hard target. Figure 2 shows a typical waveform from the digitizer that contains signals from both the reference and chilled detectors. From 0 to 4 $\mu$s, the signal is from the reference detector and the remaining time from the chilled detector.

Figure 3 is a composite of 20 waveforms from the 60-MHz digitizer card from 0.25 $\mu$s before to 1.50 $\mu$s after laser fire. From 0 to approximately 0.3 $\mu$s, we can see the effect of the TEA laser discharge impulse, which occurs at 0 $\mu$s, as a repeatable oscillation in this interval. This effect prevents use of reference frequency information from the initial part of the pulse. The compositing shows that the beats are out of phase outside the 0- to 0.30-$\mu$s window, which is expected.

Figure 4 is a composite of 20 waveforms from the 60-MHz digitizer card between 16.25 and 19.0 $\mu$s after

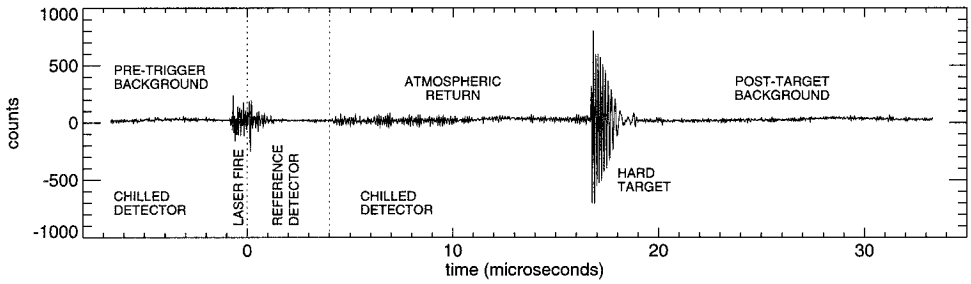


FIG. 2. Example of a typical IF waveform digitized at 60 MHz.

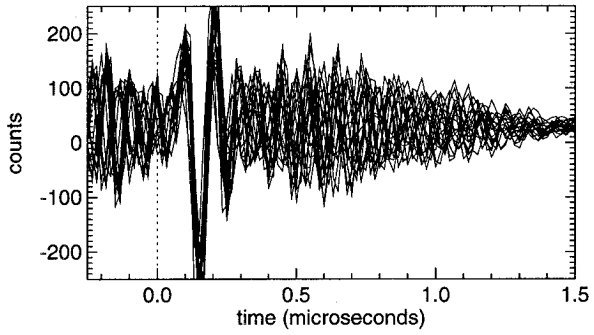


FIG. 3. A collection of superimposed waveforms from 0.25 before to 1.50 $\mu$s after laser trigger. The systematic in-phase wave from 0 to 0.3 $\mu$s is due to the TEA laser discharge.

laser fire, which contains a nearly mirror image of the pulse from the sandpaper target. Figure 5 contains power spectra from five of the sandpaper returns. These spectra each have significantly different means and a relatively broad spectral width of approximately 1.5-MHz full-width half-maximum. The spectral width can be compared with those from the NOAA $CO_2$ Doppler lidar that produces pulses with a 300-kHz spectral width mainly because of a longer cavity (3.1 m versus 0.62 m) (Post and Cupp 1990).

When the NCAR Doppler lidar operates in the CohO mode, the frequency of the transmit pulse is obtained from the reference detector via a wideband analog discriminator that is sampled at a specified time delay from the leading edge of the pulse (650 ns for the data presented in this paper). This frequency is used to control the frequency of a separate CohO that is used to mix the IF down to baseband. A manual adjustment of the sample delay time is used to empirically correct for effects related to the rapidly changing amplitude and changing frequency of the reference beat.

Figure 6 shows the $I$ and $Q$ signals created by the analog signal processor for five consecutive laser shots from 17.33 to 21.33 $\mu$s after laser fire (2600- to 3200-m range). The increase in signal amplitude beginning at 2780 m is due to the hard target. Unfortunately, during this test the amplitudes were larger than the limits of

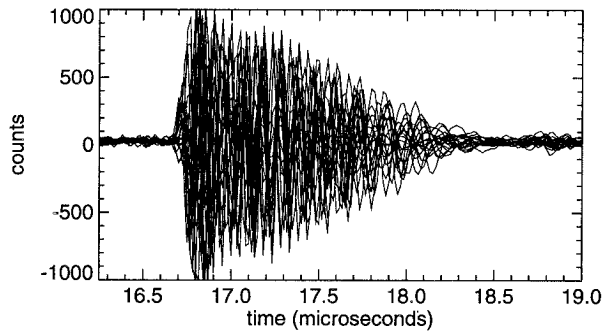


FIG. 4. A collection of superimposed waveforms from 16.25 to 19 $\mu$s after laser trigger.

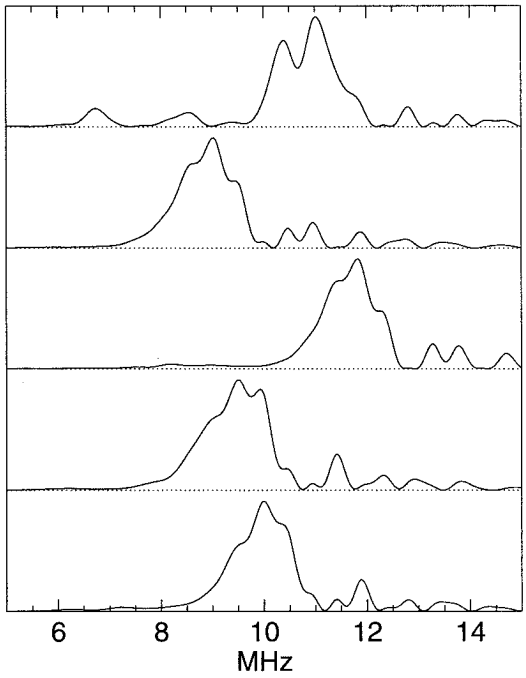


FIG. 5. Power spectra of IF data from five hard-target returns.

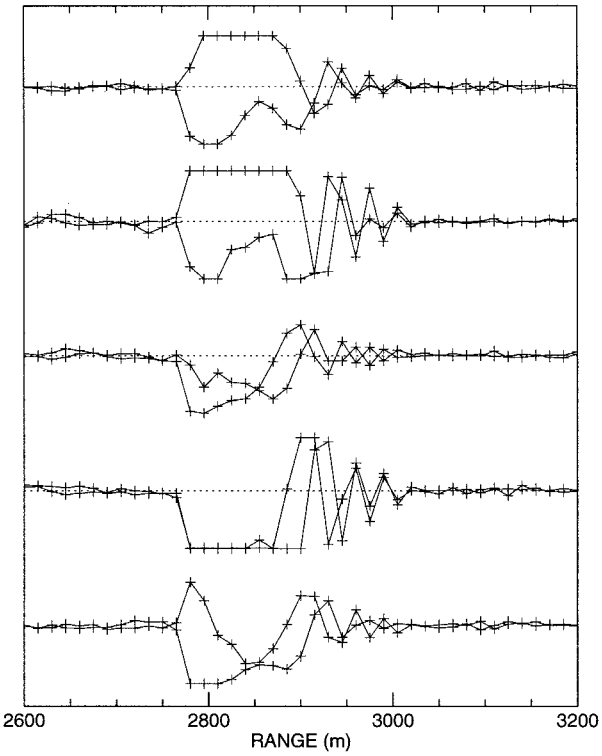


FIG. 6. In-phase and quadrature signals created by the analog signal processor for five laser pulses in the range of the sandpaper hard target. The top and bottom two are saturated.

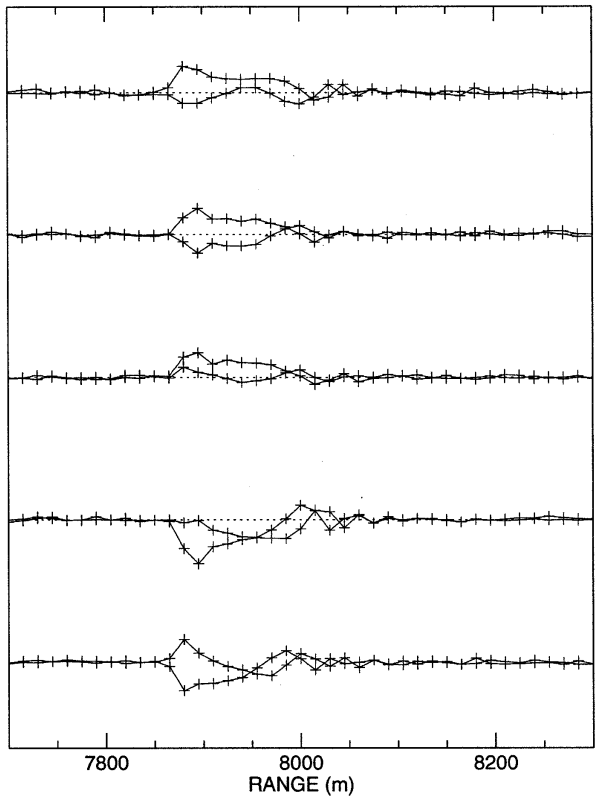


FIG. 7. Same as in Fig. 6 except in the range of the terrain target. None of these waveforms are saturated.

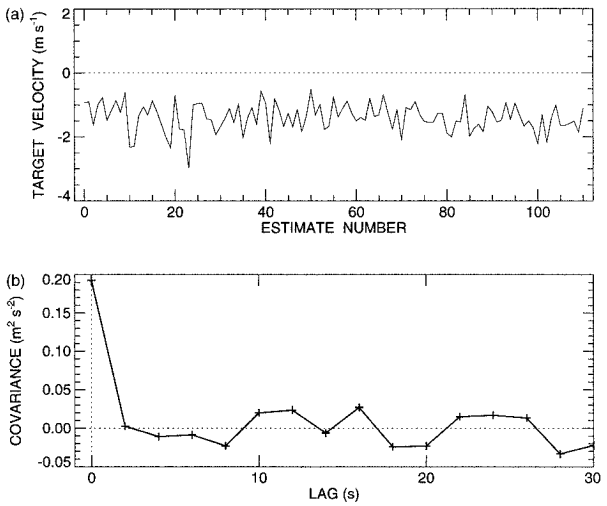


FIG. 8. (a) Time series of 20-pulse radial velocity estimates returned from the sandpaper target. $N = 111$. (b) Autocovariance function of the time series in (a). The zero-lag value equals 0.1926 $m^2 s^{-2}$ and the mean of lags 1–5 equals $-0.0039$ $m^2 s^{-2}$.

digitization. Thus, the sandpaper target *I* and *Q* data are clipped on most shots; in Fig. 6, the top two and bottom two shots are contaminated by this effect.

Fortunately, *I* and *Q* signals from the terrain target at the 7.75-km range were low enough in amplitude to rarely saturate the digitizer. Figure 7 shows the *I* and *Q* signals from five consective laser shots from the terrain target at 7.75 km (51.33–55.33 $\mu$s).

An important step in performance verification is to compare the experimental uncorrelated variance in the radial velocity estimate with theoretical predictions. For the theoretical values we used the formulation of Schwiesow and Spowart (1996), which is based on work by Doviak and Zrnić (1993). Data in Fig. 5 indicate a spectral width of the transmitted pulse of $0.75 \pm 0.1$ MHz (Gaussian half-width), which gives a normalized spectrum width of 0.0773. With this value, we calculate a correlation coefficient $\rho(T_s)$ of 0.79. For $M = 15$ samples processed per range resolution element, the reduction factor of variance *R* [Doviak and Zrnić 1993, Eq. (6.12)] is 2.45 (without approximations). Averaging 20 independent estimates, we predict a standard deviation of the velocity estimate of 0.42 m $s^{-1}$ in the limit of high SNR. At an SNR of 10 dB, the standard deviation is predicted to be 0.45 m $s^{-1}$.

For the experimental estimate of uncorrelated variance we compute the autocovariance functions (ACFs) of time series of radial velocity and subtract the first lag value from the zero lag value. The analysis is complicated because of the saturated *I* and *Q* data from the hard-target returns, as shown in Fig. 6. We chose to use the 10-MHz *I* and *Q* data over the 60-MHz IF data because the *I* and *Q* data are used for operational measurements and capable of recording every laser shot.

Figure 8a is a time series of radial velocity estimates ($n = 111$), each obtained from 20 laser pulses and 15 pairs of I and Q data that span 225-m range or 1.5-$\mu$s sample time. This ensures that the entire pulse returned from the hard target is incorporated in the velocity estimate. The time series is the velocity estimate for the gate that occurs 0.6 $\mu$s after the leading edge of the hard-target return (2780 m). Laser shots that produced a saturated *I* or *Q* value were excluded. The variance of the time series is 0.1926 $m^2 s^{-2}$ (standard deviation of 0.44 m $s^{-1}$), which exceeds the theoretical prediction by only 5%. (Since many pulses were excluded because of clipping, the velocity estimates are not distributed evenly in time and could not be used for estimates of correlated error.) The mean of the data in Fig. 8a is $-1.39$ m $s^{-1}$. We discuss the probable cause of this bias in the next section.

To test for correlated errors (i.e., drifting LO frequency), we used velocity estimates from a terrain return that began at 7880 m and only occasionally saturated a digitizer. Figure 9a is the time series of radial velocity estimates of the gate corresponding to 0.7 $\mu$s after the pulse encounters the terrain target. The ACF of this time series is shown as Fig. 9b. Unlike the radial velocity estimates in Fig. 8, those in Fig. 9a ($n = 464$) are distributed evenly in time (every 2 s), although a few pulses were excluded because of saturation. Thus, for the time series in Fig. 9a, the average number of laser shots used

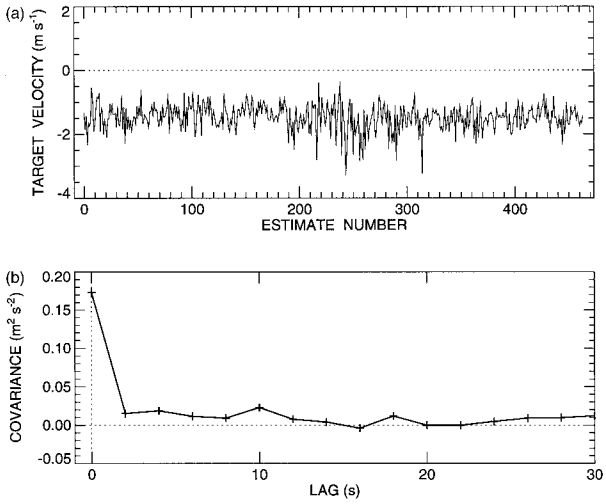


FIG. 9. (a) Time series of 20-pulse radial velocity estimates returned from the sandpaper target. $N = 464$. (b) Autocovariance function of the time series in (a). The zero-lag value equals 0.1731 $m^2$ $s^{-2}$ and the mean of lags 1–5 equals 0.0155 $m^2$ $s^{-2}$.

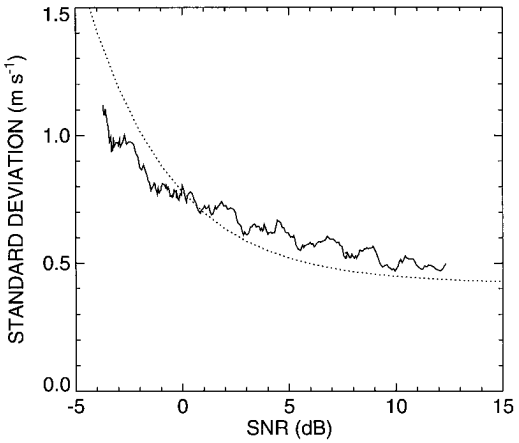


FIG. 10. Standard deviation of the lidar radial velocity as a function of wideband SNR. Solid line is from observations and dotted curve is from theory. The observations were made on 6 November 1995 at the NOAA Table Mountain experimental site, which is approximately 10 km north of Boulder, Colorado.

was 19. The peak (zero lag) of the ACF in Fig. 9b is 0.1731 $m^2$ $s^{-2}$. Figure 9b indicates that for nonzero lag, the ACF shows no significant correlation and therefore we conclude that the estimates are independent.

These values of radial velocity precision (random error) can be compared with those from other Doppler lidars. For example, Gal-Chen et al. (1992) report a standard deviation of 0.35 m $s^{-1}$ for 12 pulses with the the NOAA-ETL ground-based Doppler lidar, while Frelich et al. (1994) report a variance of 0.13 $m^2$ $s^{-2}$ for single-shot estimates from a flash-lamp-pumped 2-$\mu$m Doppler lidar operating at 5 $s^{-1}$. Schwiesow and Spowart (1996) calculate a standard devation of 0.4 m $s^{-1}$ in the limit of high SNR for the NCAR 10.6-$\mu$m Doppler lidar operating with a normalized spectrum width of 0.051, $M = 6$, and 20 pulses averaged.

To demonstrate how the random error of radial velocity changes as a function of wideband SNR, we computed ACFs for each time series starting at 1 km. The standard deviation is less than 0.5 m $s^{-1}$ at 1-km range and increases to approximately 2 m $s^{-1}$ just before the terrain target at 7865 m. It drops abruptly to 0.4 m $s^{-1}$ after the beginning of the terrain target, where the atmospheric turbulence contribution to the width vanishes and the SNR is high. This is consistent with our theoretical predictions.

Figure 10 shows the uncorrelated standard deviation as a function of SNR for actual data (solid line) and theory (dotted curve). At an SNR of 10 dB, a smoothed approximation of the data gives a standard deviation of 0.5 m $s^{-1}$, which is about 10% above the theoretical prediction. We attribute this difference to uncertainty in the frequency compensation for the difference between transmitter and LO from pulse to pulse, which is done electronically. Note in Fig. 5 that the pulse-to-pulse frequency difference is much larger than the spectral width of the transmitted pulse.

At very low SNRs, the experimental values for standard deviation fall below the theoretical prediction that contains contributions from the noise-dependent $T_2$ and $T_3$ terms (Schwiesow and Spowart 1996). We attribute this to difficulty in estimating very low SNR values. For the low SNRs the data are merely indicative of the general trend, and we consider the theoretical predictions correct.

## 4. Comparisons with an anemometer

The lidar beam was transmitted from the second floor of the NCAR Foothills Laboratory and passed approximately 10 m above a PAM II two-axis propeller anemometer mounted 10 m AGL on a tower at the 1.5-km range. Each sensor (R. M. Young Company model 27106) has a threshold speed of 0.5 m $s^{-1}$, an accuracy of 0.5 m $s^{-1}$, and a propeller distance constant of 3.3 m (Militzer 1987). The axes of the sensors are aligned north–south and east–west, and the horizontal component of the wind, parallel to the lidar line of sight, was computed for comparison with the lidar radial velocity at the 1.5-km range. The lidar data were averaged for 1-min periods to match the anemometer data. Anemometer data at higher sample rates were not available.

Measurements over 2–8 h were compared on many days during a 6-month period in 1994. In general, excellent agreement was found for wind fluctuations, with correlation coefficients as high as 0.97 for 90-min comparisons. Sometimes, however, a difference between the means (as large as 1 m $s^{-1}$) of each instrument was found. Figure 11 is an example with a correlation of 0.94 and a relatively small difference between the means (0.12 m $s^{-1}$).

Based on correlations between the mean velocity dif-

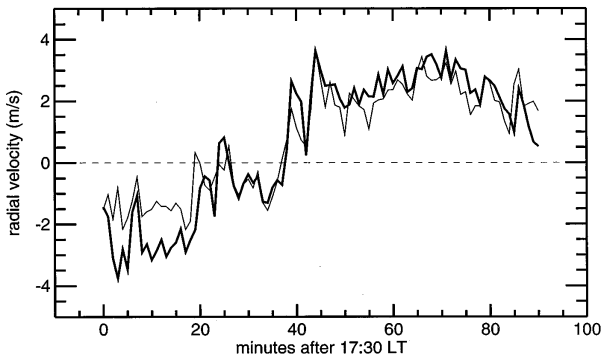


FIG. 11. Comparison of lidar radial velocity at 1.5-km range (thick line) and the corresponding component of PAM II (thin line) measured wind on 14 April 1994. The correlation coefficient is 0.94 and difference of the means is 0.12 m $s^{-1}$.

ferences and changes in laser pulse chirp, we conclude that the error in mean velocity is caused by the inability of the single-point reference frequency estimate to account for changes in the pulse chirp. For example, we were able to change the amount of velocity bias by tuning the TEA laser slightly. The tuning affects the laser gain and pulse length and hence the effective chirp changes. Although we strive to keep the TEA laser running at peak and repeatable performance, changes in room temperature, atmospheric pressure, and laser gas quality make this difficult to achieve.

## 5. Comparisons with a radar profiler

The lidar operated with the beam pointed vertically on 8 and 9 May 1994 at the NCAR Research Aviation Facility concurrently with a 915-MHz radar profiler. Examples of the lidar vertical velocity data collected on these two days are shown in the top two images in Fig. 12. The resolution of the data in Fig. 12 is 1 s temporally and 15 m vertically. The boundary layer was convective in both cases, with a few fair-weather cumulus on 8 May and cumulus clouds that increased in depth and coverage on 9 May.

The base of the cumulus appears in the middle image in Fig. 12, varying from approximately 1450 to 2000 m AGL, as a systematic negative–positive–negative velocity signature. In the image, it appears as a thin blue line followed by a broad yellow-brown and then green band. This signature is approximately 800 m deep in the vertical, consistent with the laser pulse length at approximately 10% power level. Velocity data at or above the thin blue leading edge of the signature are false and are due to the interaction of the pulse chirp and power with the extreme scattering gradient. Vertical velocities below this feature are not affected.

The profiler, part of NCAR's Integrated Sounding System (ISS) (Parsons et al. 1994), was located 100 m from the lidar and operated with a scan strategy that provided one short-pulse (700 ns) zenith profile every 200 s. Each profile was the mean of a 30-s dwell. Only short-pulse zenith profiles were used for comparison with the lidar because they best match the pulse length of the lidar. Lidar radial velocities at profiler sampling times and altitudes were averaged for 30 s. Figure 13 shows multilevel time series comparisons between the lidar and profiler on 9 May.

Table 1 summarizes the primary differences between the NCAR Doppler lidar and a 915-MHz radar profiler. Carter et al. (1995) review the history of UHF wind profiling and Ecklund et al. (1990) describe the field testing of a 915-MHz profiler. Angevine et al. (1993) and Angevine et al. (1994) use 915-MHz profiler data to measure vertical velocity variance and momentum fluxes in convective boundary layers. Strauch et al. (1987) discuss the precision and relative accuracy of profiler wind measurements.

The Weber–Wuertz quality control (QC) algorithm (Weber et al. 1993; Weber and Wuertz 1991) was applied to the profiler data used in these comparisons. Barth et al. (1995) found that this algorithm, which uses pattern recognition and a continuity model, was superior to two other QC techniques that use consensus methods. The Weber–Wuertz technique assigns a QC value, ranging from 0 to 100, to each velocity. Low QC values correspond to high-quality data. In Fig. 13, four points had QCs greater than 10 and, for these, linear-interpolation using adjacent vertical points on both sides of the omitted point was used for replacement so that continuous data would be available for cross-spectrum analysis. This is preferable to using adjacent horizontal points since there is no correlation horizontally because of the large temporal separation between values.

In addition to the profiler data acting as an independent check for the lidar measurements, the lidar data were found to be particularly useful in tuning the profiler QC algorithm parameters so that outliers were removed while retaining small-scale features in the data. Typically, the QC algorithm is set to allow a 1 m $s^{-1}$ change in velocity from one point in time to the next. However, the lidar data showed us that a 3 m $s^{-1}$ change should be allowed in order to resolve the stronger updrafts and downdrafts.

Correlation coefficients from the lidar and profiler vertical velocities were as high as 0.866 ($n = 46$) on 9 May 1994 with typical values ranging from 0.60 to 0.80. The correlation coefficients and the number of points used to compute them at each level are listed on the right side of Fig. 13. On 9 May, the vertically averaged mean lidar minus the mean profiler vertical velocities at each level from 532 to 1372 m was $-0.81$ m $s^{-1}$. Figure 14 shows the mean and variance of the profiler and averaged lidar vertical velocities as a function of altitude. Because of the volume-averaging effect of the lidar and radar samples, the variances shown are filtered versions of the true atmospheric variance. The vertical velocity data in the top two images in Fig. 12 have been

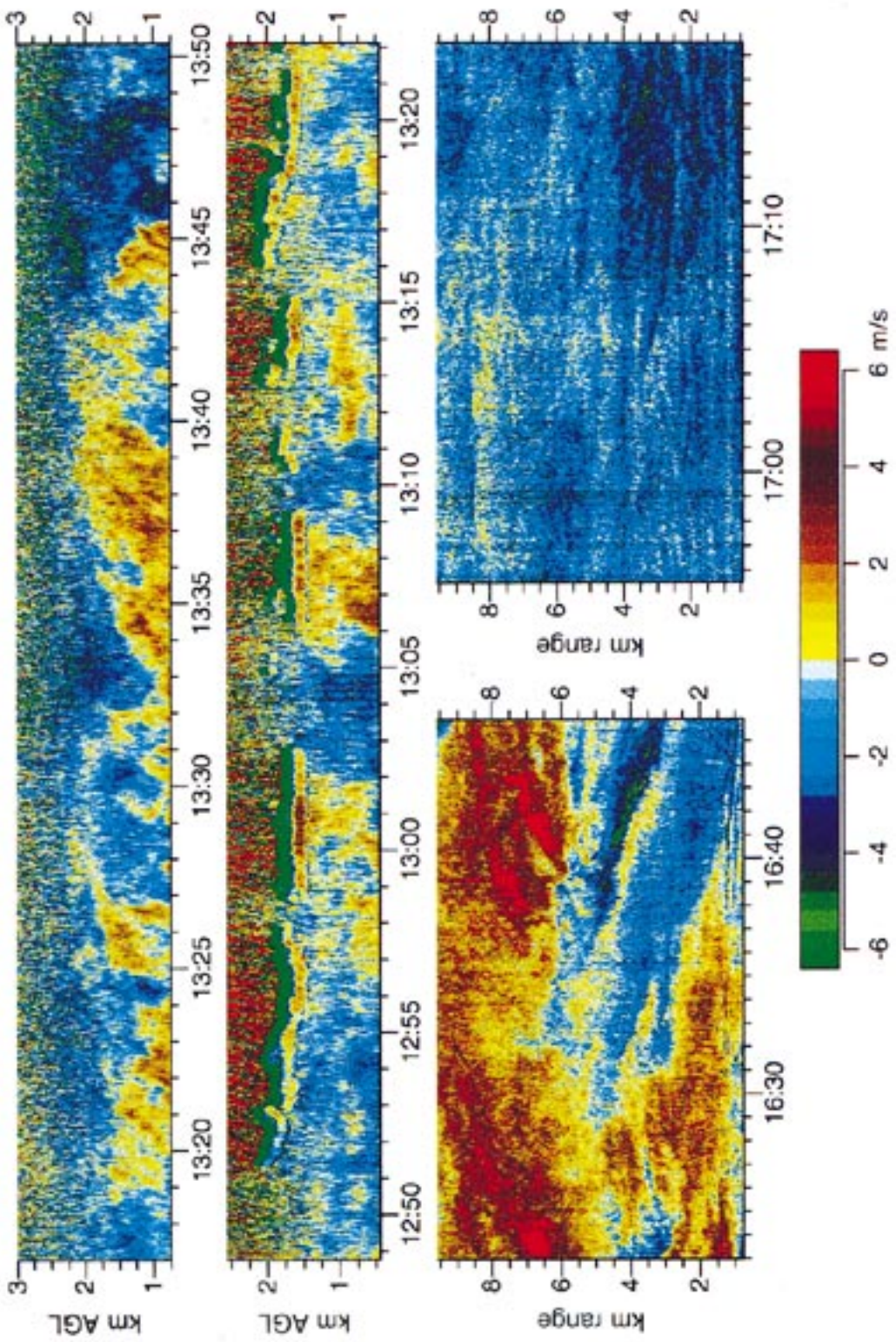


FIG. 12. Top image: time–height display of vertical velocity in a convective boundary layer as measured by the NCAR Doppler lidar on 8 May 1994. Middle image: time–height display of vertical velocity in a convective boundary layer with cumulus clouds on 9 May 1994. Cloud bases are at 1450 m AGL and higher. Lower left image: time–range display of quasi-horizontal radial velocity near the surface on 18 April 1994. The data exhibit considerable inhomogeneity. Lower right image: time–range display of quasi-horizontal radial velocity on 28 June 1994. These data are relatively homogeneous and stationary. All times are in MDT.

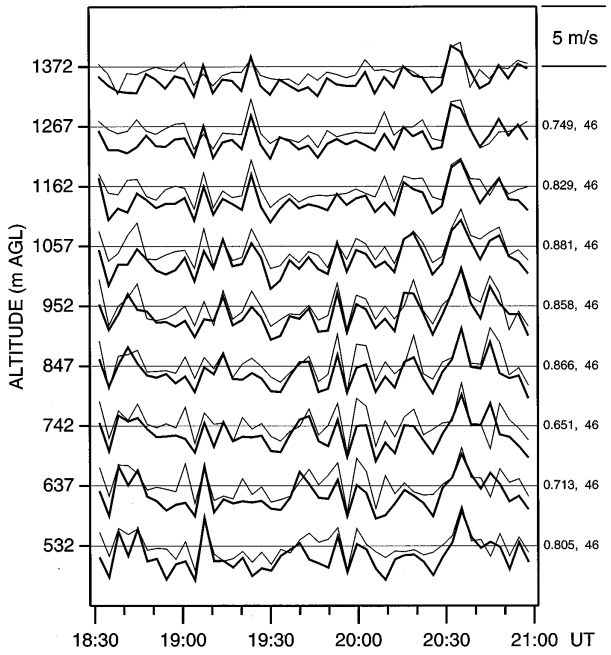


FIG. 13. Time–height comparison of lidar (thick line) and profiler (thin line) vertical velocities on 9 May 1994. Numbers to the right indicate correlation coefficient and number of points available for comparison at that altitude. Four (out of 414) profiler data points were rejected by the Weber–Wuertz QC algorithm and replaced by interpolation between adjacent vertical levels. The velocity scale is 5 m $s^{-1}$ per vertical division.

adjusted to account for the vertically averaged difference in the means on each of these days.

Significant contributions to the short-term differences between the two vertical velocity measurements are 1) different sizes of the sampling volumes and 2) the spatial separation of the two measurements. The lidar sampling volumes are long and narrow (approximately 29.7 $m^3$), while the region contributing to a profiler velocity measurement is over five orders of magnitude larger (approximately $3.5 \times 10^6$ $m^3$ for 8° beam divergence and 700-ns pulse length at 1270 m AGL). The 100-m separation of the two instruments on 8 and 9 May means that the two sampling volumes are completely different up to 1270 m AGL.

Additional factors that may affect the radial velocity correlation between the lidar and profiler are the individual SNRs of each instrument and the speed, direction, and variance of the wind. Although lidar and profiler SNRs cannot be compared directly with each other, each can be used to evaluate relative system performance under different conditions. Carter et al. (1995) discuss how radar profiler SNR is computed. Keeler et al. (1987) discuss the significant differences in interpretation of SNR between scientists with optical and radar backgrounds.

The lidar wideband SNR (in decibels) presented in Fig. 15 is defined as (Keeler and Passarelli 1990)

TABLE 1. A comparison of the NCAR 10.6-μm $CO_2$ Doppler lidar and a 915-MHz radar profiler.

| 10.6-μm NCAR $CO_2$ Doppler lidar | 915-MHz radar profiler |
|---|---|
| Middle infrared (28.3-THz frequency) | UHF (0.33-m wavelength) |
| 0.84-μs coherence time(for 1 m $s^{-1}$ velocity spectral width) | 26-ms coherence time (for 1 m $s^{-1}$ velocity spectral width) |
| 0.005° beamwidth (80 μrad full angle) | 8° beamwidth (0.14 rad full angle) |
| Pulse repetition frequencies from 0 to 30 Hz | Pulse repetition frequencies from 14 to 40 kHz |
| Relies on small particles(1–3-μm radius) for backscatter (Mie scattering) | Relies on inhomogeneities in the refractive index for backscatter (Bragg scattering) |
| High temporal resolution radial velocity estimates (0.4 m $s^{-1}$ precision for 20 laser pulses in good SNR conditions) | Lower temporal resolution radial velocity estimates (Requires approximately 30-s spectral averaging) |
| Maximum spatial dimension of sample volume is limited by pulse length (approximately 100 m) | Maximum spatial dimension is limited by beamwidth (0.14 × range) |
| Humidity causes aerosol swelling and improves SNR | Strong temperature and humidity gradients improve SNR |
| Humidity also attenuates signal | |
| Scattering gradients add error to velocity estimates because of inherent (uncontrollable) pulse frequency chirp | Scattering gradients do not affect the velocity estimates because pulse frequency is constant |
| No sidelobes | Sidelobes (vulnerable to ground clutter) |
| Asymmetric pulse amplitude | Symmetric pulse amplitude |
| No pulse phase coding | Pulse phase coding optional |
| Pulse length (0.4–1 μs) and power (40–200 mJ per pulse) depend on laser gas mixture | Pulse length selectable (0.4–3.3 μs) |
| | Pulse power depends on pulse repetition rate (3–25-W average) |
| Beam steering requires moving mirrors | Phased array antenna allows five discrete beam angles (no moving parts) |
| Full hemispherical scanning possible (30° $s^{-1}$) | |
| Requires operator attendance | Unattended operation (for a week or more) |
| One of a kind | Commercially available |

$$\text{SNR (dB)} = 10 \log_{10}(P_r/P_n), \quad (1)$$

where $P_r$ is received power and $P_n$ is noise power integrated over the frequency range that corresponds to the velocity measurement range of the lidar ±26 m $s^{-1}$. We define $P_n$ as the mean signal power in the absence of atmospheric return (often referred to as the *background* level with telescope open) and

$$P_r \propto \overline{(I^2 + Q^2)} - P_n.$$

Figure 15 shows the mean SNR profiles (in decibels) for the lidar and profiler during the comparison period on 9 May 1994.

Figure 16 contains the mean vertical velocity energy spectra, coherence, and phase angle (e.g., Stull 1988) for the lidar and profiler data shown in Fig. 13. These results were achieved by computing the cross-spectra of the two time series at each of the nine vertical levels.

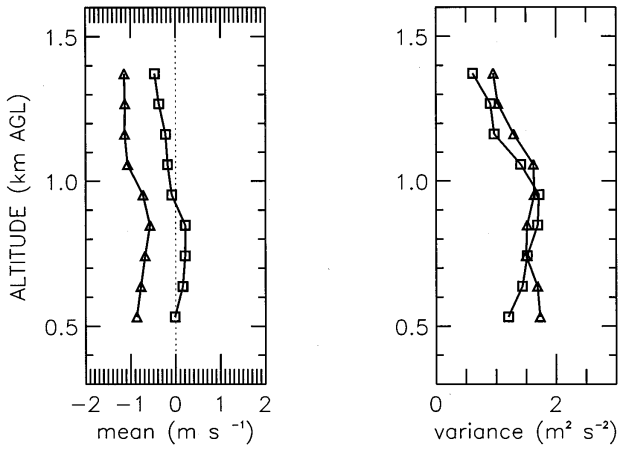


FIG. 14. Mean and variance of vertical velocity as a function of altitude for lidar (triangles) and profiler (squares) on 9 May 1994. The vertically averaged difference is 0.81 m $s^{-1}$, and the standard deviation of the differences is 0.11 m $s^{-1}$.

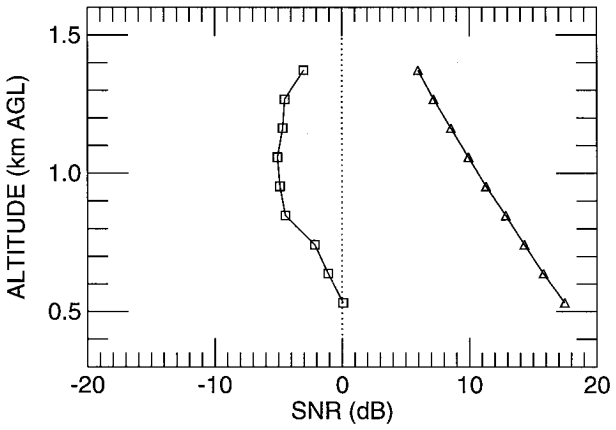


FIG. 15. Average wideband SNR for the lidar (triangles) and profiler (squares) on 9 May 1994 during the comparison period shown in Fig. 13.

The cross-spectra are then averaged over three Fourier modes and all nine levels to increase the significance of the results.

The dashed horizontal line on the coherence plot (middle panel) in Fig. 16 is the value that would be exceeded by 1% of the coherence estimates of two time series that are uncorrelated with each other. All of the coherence estimates of the two vertical velocities are well above this level. The high values of coherence and the nearly zero phase angle indicate that both instruments are measuring the actual vertical velocity at all the resolved scales.

We also evaluate the spectra of the lidar vertical velocity. Figure 17 shows the lidar spectral density multiplied by frequency for a 3-h lidar-measured vertical-velocity time series at 990 m AGL on 9 May 1994. This series consists of 10 800 1-s observations, each of which is the average of 10 laser shots. The power spectrum is smoothed over 10 equal logarithmic intervals (Kaimal and Finnigan 1994). The vertical lines on the spectrum show the 80% confidence interval.

The spectrum has a maximum at approximately $10^{-3}$ Hz (1000-s period). From this point to approximately a 30-s period, the power spectrum has an $f^{-2/3}$ slope, which is consistent with the inertial subrange turbulence hypothesis. At frequencies higher than 0.03 Hz (33-s period), the power spectrum has an $f^{+1}$ slope, which is characteristic of random uncorrelated noise.

## 6. Internal consistency

To test the lidar data for internal consistency, a 2D field (time versus range) of radial velocity data with the beam in a near-horizontal position was identified where the fluctuations appeared homogeneous and stationary. The data were collected on 28 June 1994 from the NCAR Foothills Laboratory with the beam directed at

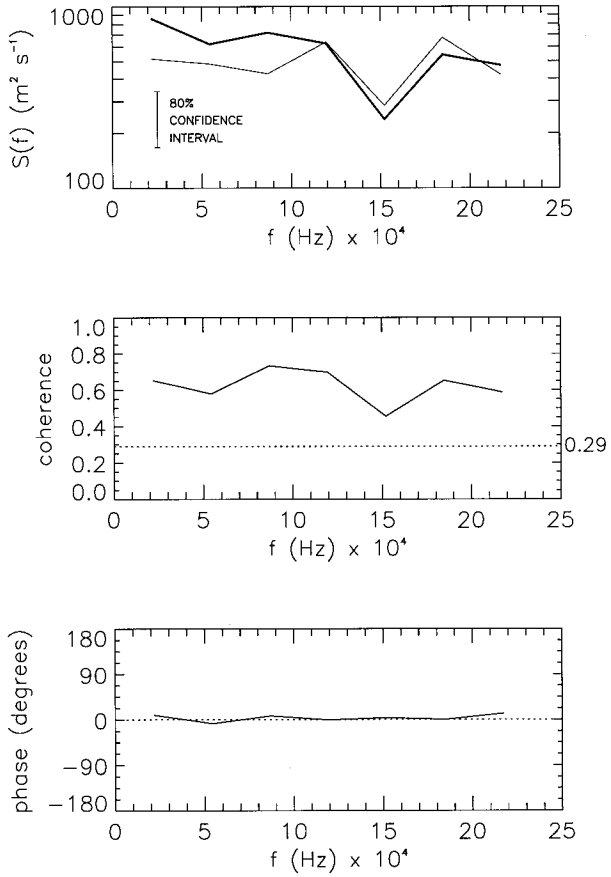


FIG. 16. Energy spectra (top; thick line is lidar, thin line is profiler), coherence (middle), and phase angle (bottom) for the vertical velocities shown in Fig. 13. The vertical bar in the top panel represents the 80% confidence interval for the spectral estimates.

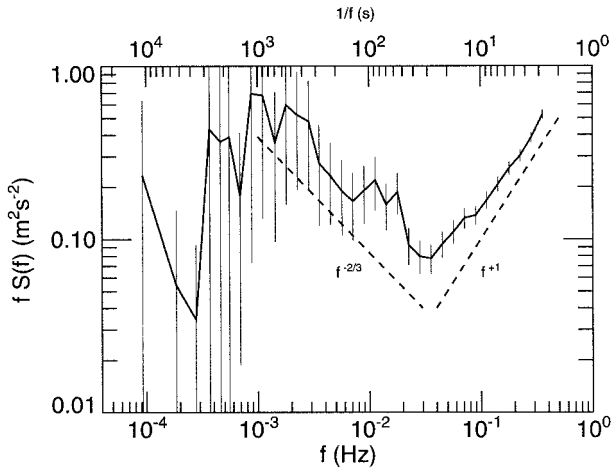


FIG. 17. Power spectrum of a 3-h time series of vertical velocity at 990 m AGL measured by the Doppler lidar on 9 May 1994. The time series consisted of 10 800 1-s samples that were computed using single-lag complex autocovariance processing applied to seven pairs (105 m) of *I* and *Q* data in the vertical. The power spectrum was smoothed over 10 equal logarithmic intervals before plotting. The vertical lines represent the 80% confidence interval for the spectral estimates.

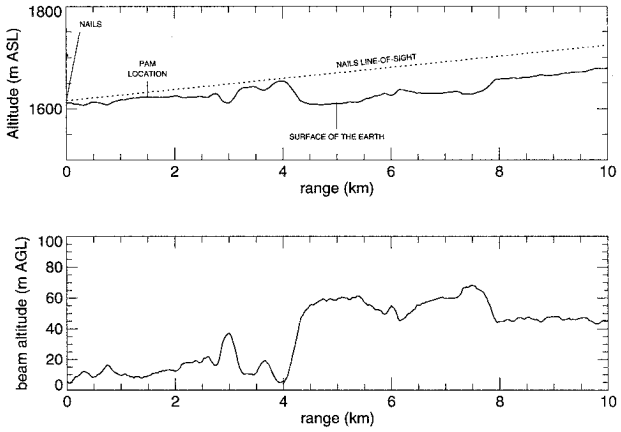


FIG. 18. NCAR Doppler lidar line of sight from the Foothills Laboratory in Boulder with respect to the underlying terrain.

approximately 0.6° elevation angle and 344° azimuth angle along the path shown in Fig. 18. The terrain data shown in Fig. 18 were obtained from a U.S. Geological Survey digital relief map of the Boulder area with 30-m resolution. During a 22-min period in the afternoon (1655:30 to 1717:30 MDT), the radial velocity display (see lower right image in Fig. 12) indicated a relatively homogeneous pattern at all ranges (500 to 9500 m) with almost no temporal change. The corresponding aerosol distribution showed no large scattering gradients. This condition is necessary to avoid the effect of pulse chirp in inhomogeneous scattering conditions. During this period, the mean horizontal wind vector at the PAM II station was from 18° at 3.2 m $s^{-1}$.

The lower left image in Fig. 12 is presented for comparison with the lower right image in Fig. 12. It shows large temporal and spatial variability in the radial velocity field as a cold front approached the Boulder area from the north on 18 April 1994. For all the velocity data presented in this paper, positive values (warm colors) indicate motion away from the lidar.

As Fig. 18 indicates, the lidar beam is not at a constant altitude above the ground. For most of the first 4 km of data, the ground is less than 20 m below the beam. After the 4-km range the beam altitude averages approximately 50 m AGL. Since the lidar radial velocity data along this line are essentially horizontal, moments of the velocities are not strongly dependent upon height above the ground. However, sharp changes in the terrain, such as the steep hill near 4 km, could enhance turbulence in that region. Figure 19 contains the mean and variance of the radial velocity as a function of range during the 22-min sample of data. The variance from 2.5- to 4-km range is approximately twice that elsewhere, suggesting that turbulence is being generated as the flow passes over the hill near 4 km. Because the mean flow during that time was from 18° and the beam azimuth was 344°, the region of enhanced variability is consistent with the expected location of a wake perturbation. This observation demonstrates the value of Doppler lidar for measuring the variation of turbulence over irregular terrain.

Although this feature suggests some degree of horizontal inhomogeneity in the velocity variance, we nevertheless use the data to examine the correlating effects of the laser pulse and signal processing. Profiles of mean SNR for the horizontal data were not available because all of the recorded I and Q data in these cases were in the presence of significant atmospheric scattering and a background was not recorded. (For the vertical data, we simply used I and Q data from 10-km range as background.)

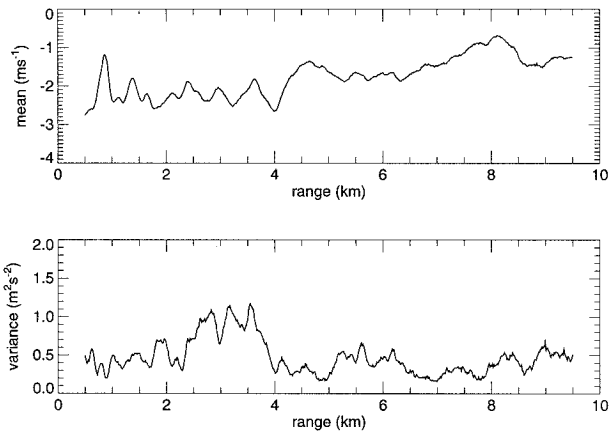


FIG. 19. Mean (top) and variance (bottom) of quasi-horizontal lidar radial velocities as a function of range from 1655:30 to 1717:30 MDT on 28 June 1994.

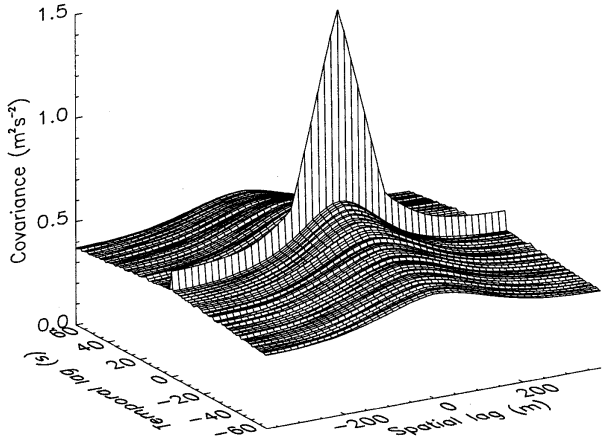


FIG. 20. Two-dimensional ACF of quasi-horizontal lidar radial velocities from 500- to 9500-m range and 1655:30 to 1717:30 MDT on 28 June 1994. The radial velocity field consisted of 1320 1-s profiles. Each profile contained 600 15-m radial-velocity estimates that were computing using a sliding seven-point single-lag complex ACF processing algorithm.

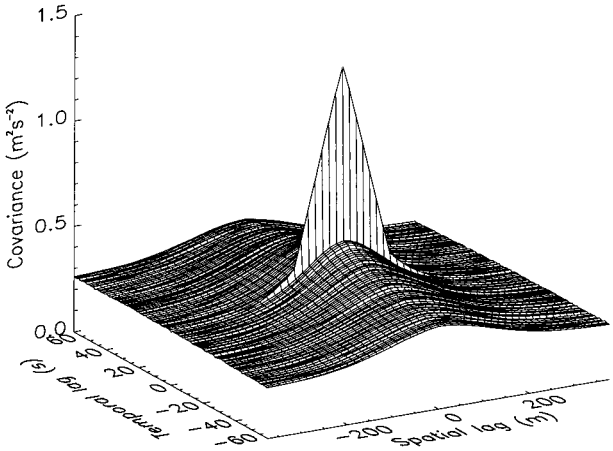


FIG. 21. Two-dimensional ACF evaluated after the mean of each profile has been subtracted to show correlating effect of pulse length.

### *a. Autocovariance functions*

Two-dimensional auto ACFs presented here (Figs. 20 and 21) were computed by inverse-Fourier transforming the power spectra of the radial-velocity field. The 2D ACF shows a peak at zero spatial and temporal lag of 1.62 $m^2\ s^{-2}$, which is the variance contributed by uncorrelated random noise and correlated fluctuations. [We refer the reader to Bendat and Piersol (1986), Lumley and Panofsky (1964), or Kaimal and Finnigan (1994) for more information on time series analysis and ACFs.] The upward-sloping ACF field surrounding the ''fin'' at zero spatial lag and small temporal lag is due to real correlations of the radial wind field measured by the lidar and correlated errors in the velocity estimates (which we conclude are small from hard-target test results). Additional correlation in the spatial direction is contributed by the single-lag complex autocovariance processing algorithm (0–105-m lag), laser pulse length (0–210-m lag), detector bandwidth, and the turbulent velocity field. Electronic noise contributes to the magnitude of the uncorrelated maximum at the center. Volume averaging, on the other hand, reduces the velocity variance. Thus, the velocity variances reported here are filtered versions of the true atmospheric velocity variance.

If measurement errors are negligible (correlated or uncorrelated), the ACF at zero spatial and temporal lag is a reasonable approximation to the sample-volume filtered variance of the wind. Here, the variance can be estimated by extrapolating the ACF from small temporal lag to zero lag to eliminate uncorrelated contributions to the variance. In Fig. 20, and this procedure gives a value of 0.71 $m^2\ s^{-2}$. Thus, about 0.9 $m^2\ s^{-2}$ is due to uncorrelated fluctuations. The relative contribution of correlated and uncorrelated fluctuations mostly depend on the average SNR over the velocity field, the spatial averaging, and the true atmospheric velocity variance.

To show the correlating effect of the laser pulse length beyond the correlation caused by signal processing in the spatial direction, the 2D ACF calculation was repeated with the mean of each velocity profile removed before transformation. The result is shown in Fig. 21. The fin along the zero temporal lag is removed for lags greater than 195 m and less than −195 m. This enhanced correlation was present in Fig. 20 but not obvious because of the enhanced correlation along the entire length of the zero-temporal-lag ACF. Because we know that the processing scheme does not introduce significant correlations in the data beyond ±105 m, we conclude that the enhancement from −195 to −105 m, and from 105 to 195 m is due to the correlating effect of the tail of the laser pulse.

### *b. Power spectra*

In this section we present the spatial power spectrum transfer function and show that the temporal and spatial power spectra of radial velocities are similar. The velocity spectra presented in this section are plotted using semilog graphs with discrete spectral energy $S(f)$ multiplied by frequency $f$. We chose this style (instead of, e.g., log–log plots) because of the occasional negative values that occur in corrected spectra and because the area under any portion of the curve is equal to the variance within that spectral range. The spectra presented in this section have been smoothed over 25 equal logarithmic frequency intervals, rather than 10 as in the previous section.

The high-frequency end of a power spectrum of a time series of radial velocities is dominated by random noise, which has a +1 spectral slope (shown in Fig. 17). The low-frequency end of that spectrum is dominated by atmospheric motions. The contribution of ran-

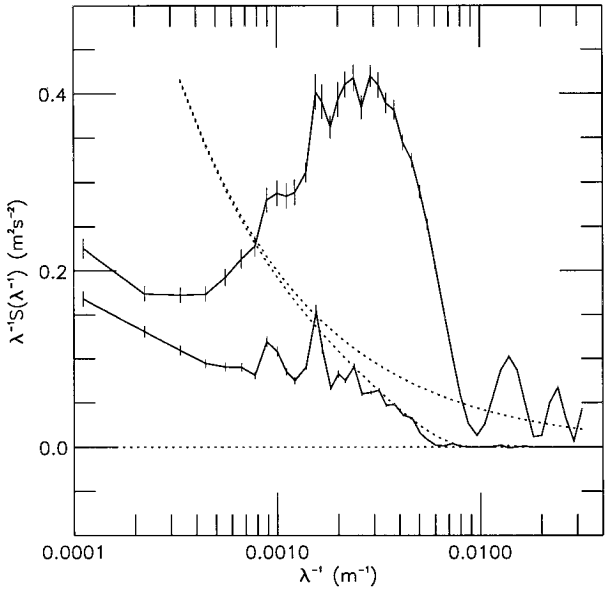


FIG. 22. Mean spatial power spectra of lidar radial velocities. Upper solid curve contains no corrections. Lower solid curve is corrected for the effect of random noise and the signal processing scheme. Vertical lines on the solid curves are 80% confidence intervals. Both curved dashed lines obey the $\lambda^{5/3}$ power law.

dom noise can be approximately removed by subtracting this constant noise level from the entire spectrum.

Spatial spectra contain steep valleys due to the effects of the ACF signal processing. Therefore, windowing has been applied to the velocity profiles before transformation to prevent leakage of spectral energy into adjacent frequency bins. The upper solid curve in Fig. 22 is the mean spatial power spectrum of the velocity, which was obtained by first filtering each velocity record with the Hanning window (Press et al. 1989), then computing its spectrum. The 1320 spectra were then averaged over the 22-min period. The vertical lines on the spectra in Fig. 22 represent the 80% confidence interval.

Because the measurement is contaminated by noise, we expect the transfer function, which is the ratio of the true (atmospheric) power spectrum to the measured power spectrum, to be less than one—especially at high frequencies. To determine the transfer function, we use the Wiener–Khintchine theorem (Lumley and Panofsky 1964) to transform the fin part of the spatial ACF shown in Fig. 21. The fin of the ACF is obtained by subtracting either of the neighboring spatial ACFs, which are not contaminated by uncorrelated noise and the signal processing scheme, from the spatial ACF at zero temporal lag. The fin is then Fourier transformed and divided by the variance to obtain a transfer function. This transfer function is plotted as the solid line in Fig. 23.

If we assume that the effect of the processing scheme is approximately equivalent to a 105-m running mean, the transfer function is

$$S(\lambda^{-1}) = \mathrm{sinc}^2(105\pi/\lambda), \qquad (2)$$

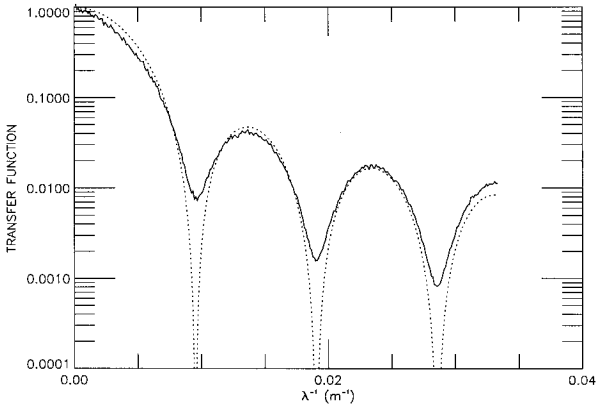


FIG. 23. Velocity profile transfer functions. The solid line is estimated from the data. The dashed line is equivalent to the transfer function produced by a 105-m running mean.

where

$$\mathrm{sinc}(x) = \sin(x)/x.$$

Equation (2) is the dashed line in Fig. 23. The two transfer functions are very similar, which confirms that the fin is due to the signal-processing scheme approximated by Eq. (2). By dividing the mean spatial cospectrum by the transfer function Eq. (2), we can better estimate the ''true'' atmospheric spectrum not altered by noise and the signal-processing scheme.

Figure 24 is a comparison of the corrected spatial and temporal power spectra. The abscissa of the temporal spectrum is obtained by dividing the frequencies by the component of the mean wind speed parallel to the lidar beam. As expected, the two power spectra are quite similar, which demonstrates the efficacy of the tech-

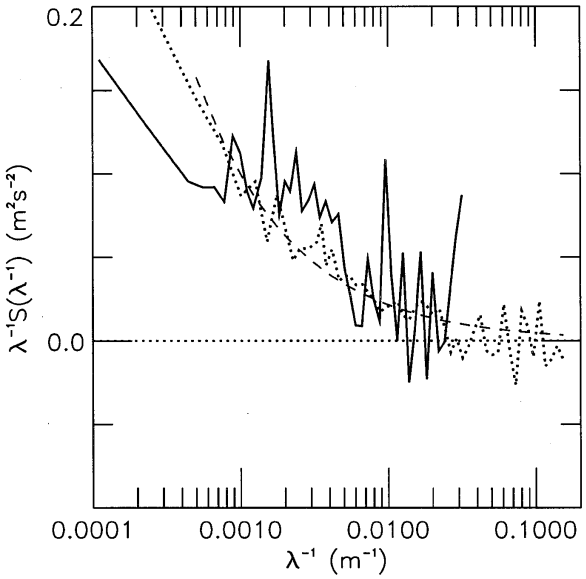


FIG. 24. Comparison of corrected spatial (solid) and temporal (dotted) spectra. The curved dashed line is proportional to $\lambda^{5/3}$.

niques for correcting the spectra in both temporal and spatial dimensions with resulting consistency of the corrected radial velocity spectra in both the temporal and spatial dimensions.

## 7. Conclusions

Validation of the NCAR $CO_2$ Doppler lidar's radial velocity measurement capability included 1) hard-target testing, 2) comparison with anemometer data, 3) comparison with 915-MHz profiler data, and 4) spectral analysis of fixed-beam radial velocity measurements.

Nonmoving hard-target data show that correlated errors in the radial velocity measurement are very small (negligible LO frequency drift) and that the random error of the hard-target velocity is approximately 0.4 m $s^{-1}$ using an average of 20 laser pulses and 1.5 $\mu$s of 10-MHz $I$ and $Q$ data, and single-lag complex autocovariance processing. Comparison of clear air radial velocity (averaged over periods of at least 30 s) with those from an anemometer and a 915-MHz radar profiler demonstrate good agreement for turbulent wind fluctuations but also indicate that the lidar data can be biased by as much as 1–2 m $s^{-1}$. We conclude that the error in mean velocity is caused by the inability of the single-point reference frequency estimate to account for changes in pulse chirp.

Spectral analysis of Doppler lidar radial velocities show that a $-5/3$ spectrum can be seen in vertical velocity data from strong convective boundary layers for periods larger than about 30 s. Two-dimensional autocovariance functions of horizontal fixed-beam data show the correlating effect of the signal processing and laser pulse. The correlating effect of the single-lag complex ACF processing is approximately equal to that of a running mean of equivalent length. We have also compared temporal and spatial power spectra of the fixed-beam data and shown that they are similar.

Despite modest pulse power, relatively large frequency chirp, and two currently unresolved engineering problems (parasitic interferometer and velocity bias), we have shown that the NCAR $CO_2$ Doppler lidar can make good radial velocity measurements under adequate SNR conditions. Its performance could be improved substantially by eliminating the parasitic interferometer and replacing the current analog signal processor with one that utilizes state-of-the-art digital electronics. However, even in its current configuration, the lidar remains useful for studies that require remote measurements of wind, such as monitoring flow over complex terrain or boundary layer turbulence structure.

*Acknowledgments.* The authors thank Mike Spowart for designing the Doppler lidar analog signal processor, Herminio Avila for technical assistance with the lidar, and Steve Cohn for discussions on the profiler. We also thank Barry Rye, Dave Parsons, Mike Hardesty, Dusan Zrnić, and the anonymous reviewers for their helpful comments on the manuscript.

REFERENCES

Angevine, W. M., S. K. Avery, W. L. Ecklund, and D. A. Carter, 1993: Fluxes of heat and momentum measured with a boundary-layer wind profiler radar–radio acoustic sounding system. *J. Appl. Meteor.,* **32,** 73–80.

——, R. J. Doviak, and Z. Sorbjan, 1994: Remote sensing of vertical velocity variance and surface heat flux in a convective boundary layer. *J. Appl. Meteor.,* **33,** 977–983.

Banta, R. M., L. D. Olivier, and J. M. Intrieri, 1990: Doppler lidar observations of the 9 January 1989 severe downslope windstorm in Boulder, Colorado. Preprints, *Fifth Conf. on Mountain Meteorology,* Boulder, CO, Amer. Meteor. Soc., 68–69.

——, ——, and W. D. Neff, 1991: Doppler lidar observations of air flow in the Grand Canyon. Preprints, *84th Annual Meeting of the AWMA,* Vol. 2, *Atmospheric Monitoring and Measurement,* Vancouver, BC, Canada, Air and Waste Management Association, 91-47.11.

——, ——, E. T. Holloway, B. W. Bartram, R. E. Cupp, and M. J. Post, 1992: Smoke-column observations from two forest fires using Doppler lidar and Doppler radar. *J. Appl. Meteor.,* **31,** 1328–1349.

——, ——, and R. M. Hardesty, 1993a: Doppler lidar and mesoscale atmospheric flows. *Proc. Seventh Conf. on Coherent Laser Radar: Applications and Technology Topical Meeting,* Paris, France, Optical Society of America, 147–149.

——, ——, and D. H. Levinson, 1993b: Evolution of the Monterey Bay sea breeze as observed by pulsed Doppler lidar. *J. Atmos. Sci.,* **50,** 3959–3982.

Barth, M. F., P. A. Miller, D. W. van de Kamp, B. E. Schwartz, R. B. Chadwick, B. L. Weber, and D. B. Wuertz, 1995: An evaluation of real-time quality control techniques applied to subhourly wind profiler data. Preprints, *Ninth Symp. on Meteorological Observations and Instrumentation,* Charlotte, NC, Amer. Meteor. Soc., 453–458.

Bendat, J. S., and A. G. Pierson, 1986: *Random Data: Analysis and Measurement Procedures.* 2d ed. John Wiley and Sons, 566 pp.

Benedetti-Michelangeli, G., F. Congeduti, and G. Fiocco, 1972: Measurement of aerosol motion and wind velocity in the lower troposphere by Doppler optical radar. *J. Atmos. Sci.,* **29,** 906–910.

Bilbro, J., G. Fichtl, D. Fitzjarrald, M. Krause, and R. Lee, 1984: Airborne Doppler lidar wind field measurements. *Bull. Amer. Meteor. Soc.,* **65,** 348–359.

——, C. DiMarzio, D. Fitzjarrald, S. Johnson, and W. Jones, 1986: Airborne Doppler lidar measurements. *Appl. Opt.,* **25,** 3952–3960.

Blumen, W., and J. E. Hart, 1988: Airborne Doppler lidar wind field measurements of waves in the lee of Mount Shasta. *J. Atmos. Sci.,* **45,** 1571–1583.

Brewer, W. A., and R. M. Hardesty, 1995: Development of a dual-wavelength $CO_2$ mini-MOPA Doppler lidar. *Coherent Laser Radar,* 1995 OSA Technical Digest Series, Vol. 19, Optical Society of America, 293–296.

Carroll, J. J., 1986: Accuracy of wind measurements using an airborne Doppler lidar. *J. Atmos. Oceanic Technol.,* **3,** 3–11.

Carter, D. A., K. S. Gage, W. L. Ecklund, W. M. Angevine, P. E. Johnson, A. C. Riddle, J. Wilson, and C. R. Williams, 1995: Developments in UHF lower tropospheric wind profiling at NOAA's Aeronomy Laboratory. *Radio Sci.,* **30,** 977–1001.

Cliff, W. C., and J. R. Skarda, 1987: Atmospheric lateral and longitudinal turbulent length scales (measured at 600 to 800 meters above grade level). *Turbulence Measurements and Flow Modeling,* C. J. Chen, L. D. Chen, and F. M. Holly Jr., Eds., Hemisphere Publishing, 89–98.

Congeduti, F., G. Fiocco, A. Adriani, and G. Guarrella, 1981: Vertical

wind velocity measurements by a Doppler lidar and comparisons with a Doppler sodar. *Appl. Opt.,* **20,** 2048–2054.

Doviak, R. J., and D. S. Zrnić, 1993: *Doppler Radar and Weather Observations.* 2d ed. Academic Press, 562 pp.

Eberhard, W. L., R. E. Cupp, and K. R. Healy, 1989: Doppler lidar measurement of profiles of turbulence and momentum flux. *J. Atmos. Oceanic Technol.,* **6,** 809–819.

Ecklund, W. L., D. A. Carter, and B. B. Balsley, 1988: A UHF wind profiler for the boundary layer: Brief description and initial results. *J. Atmos. Oceanic Technol.,* **5,** 432–441.

——, ——, ——, P. E. Currier, J. L. Green, B. L. Weber, and K. S. Gage, 1990: Field tests of a lower tropospheric wind profiler. *Radio Sci.,* **25,** 899–906.

Eilts, M. D., R. J. Doviak, and A. Sundara-Rajan, 1984: Comparison of winds, waves, and turbulence as observed by airborne lidar, ground-based radars, and instrumented tower. *Radio Sci.,* **19,** 1511–1522.

Frehlich, R., 1995: Comparison of 2- and 10-$\mu$m coherent Doppler lidar performance. *J. Atmos. Oceanic Technol.,* **12,** 415–420.

——, and M. J. Yadlowsky, 1994: Performance of mean-frequency estimators for Doppler radar and lidar. *J. Atmos. Oceanic Technol.,* **11,** 1217–1230.

——, S. M. Hannon, and S. W. Henderson, 1994: Performance of a 2-$\mu$m coherent Doppler lidar for wind measurements. *J. Atmos. Oceanic Technol.,* **11,** 1517–1528.

Gal-Chen, T., M. Xu, and W. L. Eberhard, 1992: Estimations of atmospheric boundary layer fluxes and other turbulence parameters from Doppler lidar data. *J. Geophys. Res.,* **97,** 18 409–18 423.

Grund, C. J., and M. J. Post, 1992: Design of a near-IR coherent lidar for high spatial and velocity resolution wind measurement. *Extended Abstracts, 16th Int. Laser Radar Conference,* Cambridge, MA, NASA, 405–408.

Hall, F. F., Jr., R. M. Huffaker, R. M. Hardesty, M. E. Jackson, T. R. Lawrence, M. J. Post, R. A. Richter, and B. F. Weber, 1984: Wind measurement accuracy of the NOAA pulsed infrared Doppler lidar. *Appl. Opt.,* **23,** 2503–2506.

Hannon, S. M., and J. A. Thomson, 1994: Aircraft wake vortex detection with pulsed solid-state coherent laser radar. *J. Mod. Opt.,* **41,** 2175–2196.

——, and S. W. Henderson, 1995: Wind measurement applications of coherent lidar. *Rev. Laser Eng.,* **23,** 124–130.

Hardesty, R. M., and B. F. Weber, 1987: Lidar measurement of turbulence encountered by horizontal-axis wind turbines. *J. Atmos. Oceanic Technol.,* **4,** 191–203.

Hawley, J. G., R. Targ, S. W. Henderson, C. P. Hale, M. J. Kavaya, and D. Moerder, 1993: Coherent launch-site atmospheric wind sounder: Theory and experiment. *Appl. Opt.,* **32,** 4557–4568.

Henderson, S. W., C. P. Hale, J. R. Magee, M. J. Kavaya, and A. V. Huffaker, 1991: Eye-safe coherent laser radar system at 2.1 $\mu$m using Tm, Ho:YAG lasers. *Opt. Lett.,* **16,** 773–775.

——, P. J. M. Suni, C. P. Hale, S. M. Hannon, J. R. Magee, D. L. Bruns, and E. H. Yuen, 1993: Coherent laser radar at 2 $\mu$m using solid-state lasers. *IEEE Trans. Geosci. Remote Sens.,* **31,** 4–14.

Intrieri, J. M., A. J. Bedard Jr., and R. M. Hardesty, 1990: Details of colliding thunderstorm outflows as observed by Doppler lidar. *J. Atmos. Sci.,* **47,** 1081–1097.

Kaimal, J. C., and J. J. Finnigan, 1994: *Atmospheric Boundary Layer Flows.* Oxford University Press, 289 pp.

Kavaya, M. J., S. W. Henderson, J. R. Magee, C. P. Hale, and R. M. Huffaker, 1989: Remote wind profiling with a solid-state Nd:YAG coherent lidar system. *Opt. Lett.,* **14,** 776–778.

Keeler, R. J., and R. E. Passarelli, 1990: Signal processing for atmospheric radars. *Radar in Meteorology, Battan Memorial 40th Anniversary Radar Meteorology Conference,* David Atlas, Ed., Amer. Meteor. Soc., 199–229.

——, R. J. Serafin, R. L. Schwiesow, D. H. Lenschow, J. M. Vaughan, and A. A. Woodfield, 1987: An airborne laser air motion sensing system. Part I: Concept and preliminary experiment. *J. Atmos. Oceanic Technol.,* **4,** 113–127.

Kropfli, R. A., 1986: Single Doppler radar measurements of turbulence profiles in the convective boundary layer. *J. Atmos. Oceanic Technol.,* **3,** 305–314.

Lawrence, T. R., B. F. Weber, M. J. Post, R. M. Hardesty, and R. A. Richter, 1986: Comparison of Doppler lidar, rawinsonde, and 915-MHz UHF wind profiler measurements of tropospheric winds. NOAA-TM-ERL-WPL-130, 86 pp. [Available from National Technical Information Service, Springfield, VA 22161.]

Lee, R. W., 1983: Boundary-layer observations with an airborne Doppler lidar. Preprints, *Proc. 21st Conf. on Radar Meteorology,* Edmonton, AB, Canada, Amer. Meteor. Soc., 655–657.

Lumley, J. L., and H. A. Panofsky, 1964: *The Structure of Atmospheric Turbulence.* John Wiley and Sons, 239 pp.

Mayor, S. D., 1995: Evaluation of the NCAR Doppler lidar and applications to measuring boundary layer structure. NCAR Cooperative Thesis 156, 88 pp. [Available from National Center for Atmospheric Research, Atmospheric Technology Division, Boulder, CO 80307-3000.]

——, R. L. Schwiesow, D. H. Lenschow, and C. L. Frush, 1995: Validation of radial velocity measurements from the NCAR Doppler lidar. *Coherent Laser Radar,* 1995 OSA Technical Digest Series, Vol. 19, Optical Society of America, 269–272.

McCaul, E. W., H. B. Bluestein, and R. J. Doviak, 1986: Airborne Doppler lidar techniques for observing severe thunderstorms. *Appl. Opt.,* **25,** 698–708.

Menzies, R. T., 1986: Doppler lidar atmospheric wind sensors: A comparative performance evaluation for global measurement applications from earth orbit. *Appl. Opt.,* **25,** 2546–2553.

Militzer, J. W., 1987: User's Manual 001-44PAMII-001 Version 1.0: Portable Automated Mesonet II (PAM II). [Available from National Center for Atmospheric Research, Field Observing Facility, P. O. Box 3000, Boulder, CO 80307.]

Neiman, P. J., M. A. Shapiro, R. M. Hardesty, B. B. Stankov, R. T. Lawrence, R. J. Zamora, and T. Hampel, 1988a: The pulsed coherent doppler lidar: Observations of frontal structure and the planetary boundary layer. *Mon. Wea. Rev.,* **116,** 1671–1681.

——, R. M. Hardesty, M. A. Shapiro, and R. E. Cupp, 1988b: Doppler lidar observations of a downslope windstorm. *Mon. Wea. Rev.,* **116,** 2265–2275.

Orlanski, I., 1975: A rational subdivision of scales for atmospheric processes. *Bull. Amer. Meteor. Soc.,* **56,** 527–530.

Parsons, D., and Coauthors, 1994: The Integrated Sounding System: Description and preliminary observations from TOGA COARE. *Bull. Amer. Meteor. Soc.,* **75,** 553–567.

Post, M. J., 1978: Experimental measurements of atmospheric aerosol inhomogeneities. *Opt. Lett.,* **2,** 166–168.

——, and W. D. Neff, 1986: Doppler lidar measurements of winds in a narrow mountain valley. *Bull. Amer. Meteor. Soc.,* **67,** 274–281.

——, and R. E. Cupp, 1990: Optimizing a pulsed Doppler lidar. *Appl. Opt.,* **29,** 4144–4158.

——, R. L. Schwiesow, R. E. Cupp, D. A. Haugen, and J. T. Newman, 1978: A comparison of anemometer- and lidar-sensed wind velocity data. *J. Appl. Meteor.,* **17,** 1179–1181.

Press, W. H., B. P. Flannery, S. A. Teukolsky, and W. T. Vetterling, 1989: *Numerical Recipes.* Cambridge University Press, 702 pp.

Rothermel, J., C. Kessinger, and D. L. Davis, 1985: Dual-Doppler lidar measurement of winds in the JAWS experiment. *J. Atmos. Oceanic Technol.,* **2,** 138–147.

Schwiesow, R. L., and M. P. Spowart, 1996: The NCAR airborne infrared lidar system: Status and applications. *J. Atmos. Oceanic Technol.,* **13,** 4–15.

——, S. D. Mayor, M. P. Spowart, C. L. Frush, and J. Mann, 1994: Ground-based velocity measurement performance of the NCAR Airborne Infrared Lidar System (NAILS). NCAR Tech. Note NCAR/TN-405+STR, 65 + xii pp. [Available from National Center for Atmospheric Research, Atmospheric Technology Division, Boulder, CO 80307-3000.]

Sirmans, D., and B. Bumgarner, 1975: Numerical comparison of five mean frequency estimators. *J. Appl. Meteor.*, **14,** 991–1003.

Strauch, R. G., B. L. Weber, A. S. Frisch, C. G. Little, D. A. Merritt, K. P. Moran, and D. C. Welsh, 1987: The precision and relative accuracy of profiler wind measurements. *J. Atmos. Oceanic Technol.,* **4,** 563–571.

Stull, R. B., 1988: *An Introduction to Boundary Layer Meteorology.* Kluwer Academic Publishers, 666 pp.

Weber, B. L., and D. B. Wuertz, 1991: Quality control algorithm for profiler measurements of winds and temperatures. NOAA-TM-ERL-WPL-212, 32 pp. [Available from National Technical Information Service, Springfield, VA 22161.]

——, ——, D. C. Welsh, and R. McPeek, 1993: Quality controls for profiler measurements of winds and RASS temperatures. *J. Atmos. Oceanic Technol.,* **10,** 452–464.

Willetts, D. V., and M. R. Harris, 1982: An investigation into the origin of frequency sweeping in a hybrid TEA $CO_2$ laser. *J. Phys. D: Appl. Phys.,* **15,** 51–67.

Zrnić, D. S., 1979: Estimation of spectral moments for weather echoes. *IEEE Trans. Geosci. Electron.,* **17,** 113–128.